LANGMUIR

pubs.acs.org/Langmuir Article

Formation of Nonspherical Cellulose Acetate Microparticles under Microflow

Kurumi Mori, Takaichi Watanabe,* and Tsutomu Ono*

Cite This: *Langmuir* 2024, 40, 27314−27322 Read Online

ABSTRACT: Nonspherical particles have gained significant interest owing to their unique shapes and large specific surface areas, making them suitable for a wide range of applications, such as drug delivery, catalysis, and adsorption. However, conventional methods for preparing nonspherical particles face certain limitations. In this study, we propose a simple method for fabricating nonspherical cellulose acetate (CA) microparticles using a microfluidic device in which droplets undergo rapid diffusion in a continuous aqueous phase. The influence of variations in the flow rate ratio and continuous phase composition on the dimensionless Péclet number (*Pe*) within the droplet and shape of the resultant particles is investigated. *Pe* is critical, because it indicates the balance between polymer diffusion and droplet shrinkage dynamics. Our findings reveal that increasing the flow rate ratio and reducing the methyl acetate concentration in the continuous phase lead to faster droplet shrinkage and an increased *Pe*. A high *Pe* (>100) suggests that the reduction of the droplet interface predominates over polymer diffusion, resulting in the formation of a viscous layer near the droplet surface, which subsequently leads to nonspherical particle shapes (such as bowl-like or biconcave structures). In situ time-lapse observations of droplets from the top and side of a microchannel reveal that the formation of a viscous layer near the droplet surface and the deformation of the droplet, influenced by the *z*-axis location of the droplets during particle formation, ultimately determine the final particle shape. Based on these observations, a linear correlation between the initial conditions, i.e., the *Pe* and *z*-axis location at which the viscous layer formed, is established, enabling the prediction of the particle structure. In summary, the present study enhances the understanding of shape control in microfluidic particle formation and offers a novel guideline for the fabrication of spherical and nonspherical particles.

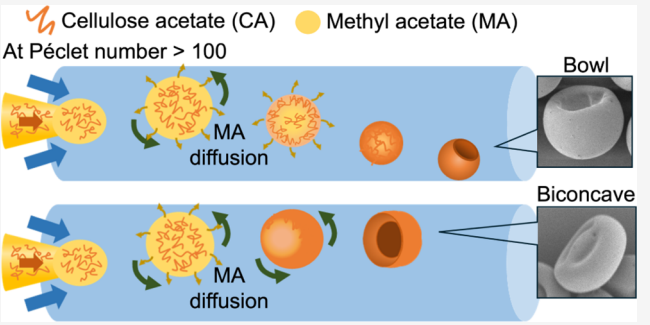

INTRODUCTION

Nonspherical particles, such as bowl-like,[1−6] doughnut-like,[7,8] and disk-like[9−11] particles, exhibit unique properties owing to their large surface areas, various aspect ratios, and optical scattering characteristics. These properties make them suitable for various applications, including drug delivery systems,[9,12,13] microwave absorption materials,[14] catalysis,[15,16] adsorbents,[17,18] and cosmetics.[19] For instance, bowl-like particles have a high volumetric packing density owing to their concave shape, which enhances the contact area between the particles and improves the electromagnetic microwave absorption performance compared to that of spherical particles.[14] Additionally, bowl-like particles mixed with metal nanoparticles improve catalytic efficiency because of their high surface-area-to-volume ratio.[20] In the biomedical field, recent studies have shown that the large surface area and concave shape of bowl-shaped particles made them highly adhesive (similar to suckers) and therefore, promising as microcarriers for gastrointestinal drug administration with long-term therapeutic effects.[12] Doughnut-like (toroidal) particles enhance the release or absorption rate of materials and improve their in vivo performance as drug carriers owing to their large surface area.[13] Disk-like particles demonstrate stronger interfacial adhesion than spherical particles because of their larger contact area,[9] which results in a high margination tendency under various shear rates of laminar blood flow.[21,22] Consequently, nonspherical particles have unique characteristics that are not found in spherical particles, leading to increased interest in their potential applications in drug delivery, catalysis, adsorption, and optics.

Various methods have been developed to prepare nonspherical polymer particles, including emulsion template polymerization, which uses emulsions or seed particles as templates for single-hole hollow particles,[5,23−25] and spray-drying, which yields bowl-shaped or dimpled particles via rapid solvent evaporation.[26,27] However, these methods have certain

Received: September 1, 2024
Revised: November 17, 2024
Accepted: December 9, 2024
Published: December 19, 2024

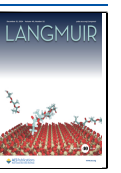

limitations. Emulsion template polymerization involves multiple steps and polymerization reactions; spray-drying is unsuitable for heat-sensitive materials such as biodegradable polymers and proteins owing to heat application although capable of producing nonspherical particles in a single step. In contrast, the emulsion solvent diffusion method[28−30] forms particles by extracting the solvent from a droplet into a continuous aqueous phase. In this method, a droplet containing a polymer and a partially water-soluble solvent is prepared; the solvent diffuses from the droplet into the aqueous phase, precipitating the polymer within the droplet and resulting in particle formation. In the last two decades, microfluidic devices have enabled the precise preparation of monodisperse droplets and the control of droplet size from nanometers to micrometers by adjusting the shear force on the dispersed phase through flow rates and channel geometry.[31−34] Combining solvent diffusion with microfluidic droplet formation is an effective method to produce polymer particles with a narrow size distribution and targeted size.[35−37] For instance, Wang et al. reported the preparation of nonspherical particles using specific fluidic conditions in microfluidic channels.[38] Ono et al. reported the formation of nonspherical particles using nonequilibrium droplets prepared in a microfluidic channel.[39] However, studies on particle shape control under flow conditions remain limited, and the factors affecting particle shape as well as the thresholds that determine shape have not yet been investigated.

In this study, we investigated the effects of preparation parameters, such as the flow rate ratio of the continuous phase to the dispersed phase and the composition of the continuous phase, on the particle shape. We then developed a correlation equation between these parameters and the dimensionless Péclet number (*Pe*) to control the particle shape using initial conditions. Specifically, we used a methyl acetate (MA) solution containing cellulose acetate (CA) as the dispersed phase and an aqueous poly(vinyl alcohol) (PVA) solution as the continuous phase. CA, a biobased polymer known for its low toxicity, biodegradability, and biocompatibility, facilitates the formation of biocompatible microparticles suitable for applications in fields such as drug delivery and cosmetics. Nonspherical CA particles, for instance, may exhibit distinct rheological behaviors and light-scattering properties compared to spherical particles. In our particle formation process, the solvent for the dispersed phase must be partially soluble but not fully miscible with the continuous phase. Therefore, we selected MA due to its significant solubility in water (25 wt % at 20 °C), as it rapidly diffuses from droplets in an O/W emulsion, facilitating the formation of both spherical and nonspherical shapes. Additionally, using MA/water mixtures with different compositions as the continuous phase allows us to control the droplet shrinkage rate over a wide range of *Pe* values. This level of control is difficult to achieve with other water-soluble polar solvents, such as ethyl acetate. When monodisperse oil-in-water (O/W) emulsion droplets were generated in the microfluidic device, MA rapidly diffused from the droplets to form CA particles. We changed *Pe* in the droplet by adjusting the flow rate ratio and MA concentration in the continuous phase and investigated their relationship with the particle shape. In addition, we observed the droplet changes over time in the microchannel to clarify the formation mechanism of the nonspherical particles. Subsequently, we established an equation to predict the particle structure using the initial fluidic conditions and *Pe*. Finally, we discussed other factors affecting the shape of the microparticles and the generalizability of this study.

EXPERIMENTAL SECTION

Materials. CA samples with different molecular weights ((1) M_w = 3.19 × 10^5, M_w/M_n = 1.96, the degree of acetylation = 55.2%, (2) M_w = 3.3 × 10^5, M_w/M_n = 2.9, the degree of acetylation = 54−56%, and (3) M_w = 2.8 × 10^5, M_w/M_n = 2.6, the degree of acetylation = 53−56%) were purchased from (1) Kanto Chemical Co., Inc., Tokyo, Japan, (2) Daicel Co., Japan, and (3) FUJIFILM Wako Pure Chemical Co., Japan. Ethyl cellulose (EC) (M_w = 1.40 × 10^5, M_w/M_n = 2.07) and poly(D,L-lactide) (PDLLA) (M_w = 5.35 × 10^3, M_w/M_n = 4.5) were purchased from Sigma-Aldrich, Japan. The molecular weight and the molecular weight distribution of CA, EC, and PDLLA were measured by gel permeation chromatography (Prominence GPC system, Shimadzu Co., Japan). *N*,*N*-dimethylformamide (for HPLC, purity of >99.7%) and chloroform (for HPLC, purity of >99.7%) were used as the eluent at a flow rate of 0.5 mL/min at 40 °C for CA and for EC and PDLLA, respectively. Polystyrene standards (PS-Polymer Kit, Tosoh, Japan) were used as references. MA and PVA (degree of polymerization = 1000, degree of saponification: 86−90 mol %) were obtained from FUJIFILM Wako Pure Chemical Corporation, Japan. All reagents were used as received without further purification. Distilled water with a resistance of 3 MΩ·cm was obtained using an Elix UV system.

Fabrication of the Microfluidic Device. A glass microfluidic device was used to prepare the O/W emulsions. The device consisted of cylindrical glass capillaries (Narishige; G-1, Japan) with inner and outer diameters of 0.6 and 1.0 mm, respectively. These capillaries were pulled by heat using a puller (PC010, Narishige) to form a tip, which was then polished with sandpaper to prepare an injection capillary with a tip inner diameter of 230 μm and a collection capillary with a tip inner diameter ranging from 335 to 600 μm. The two capillaries were placed coaxially at a separation of 150 μm in a square glass capillary (VitroCom, Cat. No. 8100) with an inner diameter of 1.0 mm. To observe the droplet changes over time, cylindrical and square glass capillaries were joined behind the collection capillary to extend the channel length to 55 cm. The capillaries were fixed on a glass plate (60 cm × 3 cm) using an epoxy adhesive (Nichiban Araldite, Japan). Plastic needles (20 G, 13 mm, Musashi Engineering, Japan) were connected to the gaps between the square glass capillaries; all inlets were connected to plastic disposable syringes (Henke Sass Wolf, Germany) with fluorinated ethylene propylene tubes (1/16 in. × 0.75 mm, VICI-Jour, Japan) (Figure S1). The syringes were attached to a syringe pump (Harvard Apparatus 33DDS) to control the flow rate. The microfluidic device was mounted on the stage of a digital microscope (VW-9000, Keyence, Japan) equipped with a high-speed camera (VW-600C, Keyence, Japan).

Preparation of CA Particles in the Microfluidic Device. A 2 wt % CA/MA solution was used as the dispersed phase, and a 1 wt % PVA solution was used as the continuous phase. The density of each solution was measured using a density meter (SVM1101, Anton Paar). Both phases were filled in syringes and fed into the microfluidic device by using a syringe pump (Harvard 33DDS, USA). Before injection of the dispersed phase, the microchannel was wetted with a continuous phase to prevent it from adhering to the microchannel walls during emulsification. The continuous phase at the junction sheared the dispersed phase, forming an O/W emulsion. Owing to the high solubility of MA in water, rapid diffusion occurred from the droplets into the continuous phase, forming CA particles (Figure 1). The flow rate ratio of the continuous phase to the dispersed phase was varied from 5 to 35, and the total flow rate was adjusted accordingly. All experiments were performed at 20−27 °C. Different microfluidic device structures ensured consistent initial droplet diameters regardless of the flow rate ratio. Table S1 lists the flow rates of the dispersed and continuous phases and the inner diameter of the collection capillary tip of the microfluidic device. The effect of MA addition to the continuous phase on the particle shape was also

https://doi.org/10.1021/acs.langmuir.4c03430
Langmuir 2024, 40, 27314−27322

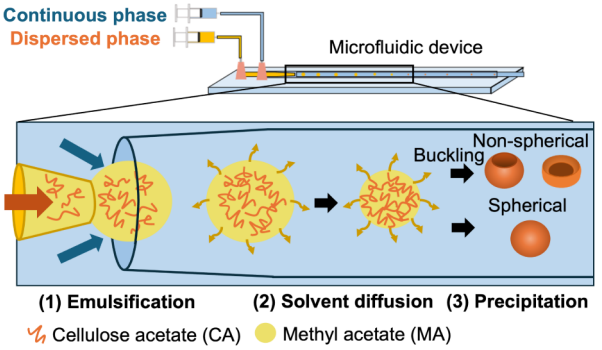

Figure 1. Schematic of CA particle preparation by solvent diffusion in a microfluidic device.

investigated by varying the MA concentration from 0 to 25 wt %. The particles were washed three times with distilled water. For scanning electron microscopy (SEM) observation (S-4700, Hitachi), CA particles dispersed in water were freeze-dried overnight (FDU-1200, EYELA).

Calculation of *Pe* in Droplets. In spray-drying, *Pe* is often used to describe the drying process of the aerosol droplets and the resulting morphology of the microparticles.[26,40] *Pe* is defined as the ratio of the solvent evaporation rate (κ), which indicates the rate of decrease in the droplet interface, to the diffusion coefficient of the suspended particles (D_i), as shown in eq 1. The evaporation rate (κ) is described by the "*R*-squared rule,"[41] which relates the initial droplet radius (R_0) to time (t), as described by eq 2.

$$Pe = \frac{\kappa}{8D_i} \tag{1}$$

$$R^2(t) = {R_0}^2(t_0) - \kappa t \tag{2}$$

The final particle morphology is determined by the dominance of the solvent evaporation rate (κ) and diffusion coefficient (D_i) in *Pe*. For instance, if $Pe \gg 1$, the droplet surface shrinks rapidly before the suspension particles can diffuse to the center of the droplet, forming a skin or shell at the droplet surface that buckles and creates nonspherical particles. Conversely, if $Pe \ll 1$, diffusion mixing is fast, keeping the particle concentration uniform within the droplet, resulting in spherical particles.

For a polymer droplet in this study, κ and D_i included in *Pe* were considered as the droplet shrinkage rate (κ) and the diffusion coefficient of the polymer (D_p) in the dispersed phase. As shown in eq 2, κ is the rate of decrease (slope) of R^2 (droplet boundary area) over time. The droplet radius (R) and time (t) were used to calculate κ by using the slope of the graph for the change in R^2 as a function of time. The diffusion coefficient (D_p) of the dispersed phase was measured by dynamic light scattering (DLS) using Malvern Zetasizer Nano ZS (Malvern Instruments) at 25 °C.

Characterization of CA Particles. The particle formation via solvent diffusion in the microchannels was observed by using the digital microscope equipped with a high-speed camera. The time evolution of the droplets in the channel was monitored by converting the channel length into the residence time. For nonspherical droplets and microparticles, the equivalent circle diameter was measured using ImageJ software (version 1.53a). Assuming complete solvent removal by diffusion, the estimated theoretical particle radius is given by eq 3.[42]

$$\text{Theoretical particle radius} = \left(\frac{x_p \rho_d}{\rho_p}\right)^{1/3} R_0 \tag{3}$$

where x_p is the mass fraction of the polymer in the initial solution, ρ_d is the density of the initial droplet, and ρ_p is the density of the polymer. The morphology of freeze-dried CA particles was observed by using SEM at a voltage of 1 kV. A sputter coater (E-1030 Ion Sputter, Hitachi) was used to coat the samples for SEM with Pd−Pt.

To obtain cross sections of CA particles, freeze-dried particles were dispersed in light-curing resin (Norland NOA81) and cured with UV light (λ = 365 nm) for 15 min. The resin was cut to create cross sections of the CA particles that were observed using SEM.

RESULTS AND DISCUSSION

Preparation of CA Particles. To prepare CA particles, we first emulsified a 2 wt % CA ($M_w = 3.19 \times 10^5$ and M_w/M_n = 1.96)/MA solution (dispersed phase) and a 1 wt % PVA aqueous solution (continuous phase) using a glass capillary microfluidic device. The flow rates for the dispersed (Q_d) and continuous phases (Q_c) were set at 20 and 100 μL/min, respectively. The high-speed camera observations of the droplet changes in Figure 2a show that the dispersed phase

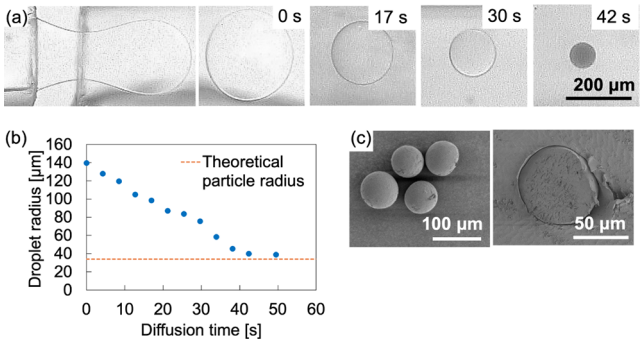

Figure 2. (a) Time evolution of a droplet flowing in a microchannel. (b) Change in the droplet radius as a function of time. The orange dashed line indicates the theoretical particle radius. (c) SEM images of particles after freeze-drying. Left: particle appearance; right: particle cross-section prepared at Q_d = 20 μL/min and Q_c = 100 μL/min.

solution is sheared by the continuous phase at the junction, forming an O/W emulsion. The droplets shrank over time, owing to the diffusion of MA from the droplets into the continuous phase, and CA particles were formed within 42 s in the microchannel. Figure 2b illustrates the change in the droplet radius as a function of time. The diffusion time represents the duration of the droplet formation. The droplet radius decreases until equilibrium is reached, indicating the formation of polymer particles. Notably, the particles were 14.6% larger than the theoretical particle diameter calculated using eq 3, probably because of water diffusion from the continuous phase into the droplets and MA diffusion from the droplets. This interpretation is supported by the cross-sectional SEM image of the freeze-dried particles in Figure 2c, which shows tiny pores inside the particles. These results confirmed that spherical particles with tiny internal pores were obtained when Q_d and Q_c values were 20 and 100 μL/min, respectively.

Effect of κ in *Pe* on Particle Shape. Nonspherical microparticles have been reported under high *Pe* conditions during spray-drying.[26,40] We then investigated whether nonspherical microparticles could be formed by increasing the droplet shrinkage rate (κ) of *Pe*. To increase the flow rate ratio (Q_c/Q_d) of the continuous to dispersed phases, which correlates with κ, we maintained a constant dispersed phase at a flow rate of Q_d = 20 μL/min and varied the continuous phase flow rate to Q_c = 100, 200, and 700 μL/min. Figure 3 shows the droplet changes over time in the microchannel. As the continuous phase flow rate increased (increasing the flow rate ratio), polymer precipitation occurred more rapidly. As discussed, spherical particles were obtained at Q_c = 100 μL/

https://doi.org/10.1021/acs.langmuir.4c03430
Langmuir 2024, 40, 27314−27322

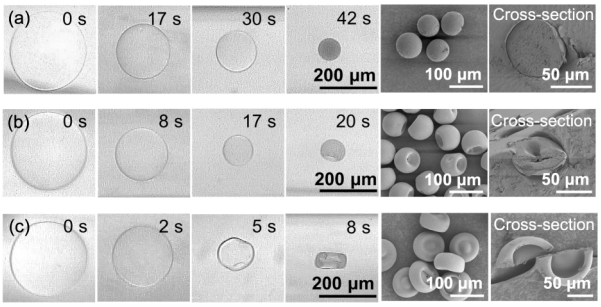

Figure 3. Particle formation process in a microchannel and SEM images of particles prepared with different Q_c ((a) 100, (b) 200, and (c) 700 μL/min) with a constant Q_d of 20 μL/min.

min (Figure 3a). In contrast, at Q_c = 200 μL/min (Figure 3b) and Q_c = 700 μL/min (Figure 3c), the droplets deformed during particle formation, resulting in nonspherical microparticles. The SEM images revealed bowl-like particles at Q_c = 200 μL/min and biconcave particles, resembling red blood cells, at Q_c = 700 μL/min. The deformation was attributed to the formation of a viscous layer near the droplet surface during particle formation. The optical digital microscopy images indicated that bowl-like particles were formed via one-directional deformation, whereas biconcave particles were formed via two-directional deformation perpendicular to the flow direction.

We next calculated the *Pe* value for each flow rate condition. κ was determined from the slope of the graph for the change in R^2 over time. As shown in Figure 4a, a lower flow rate ratio resulted in slower droplet shrinkage, because the volume ratio of the droplets (MA) to the continuous phase increased, causing the stagnation of the diffused MA around the droplets and suppressing MA diffusion. Thus, κ increased at higher flow

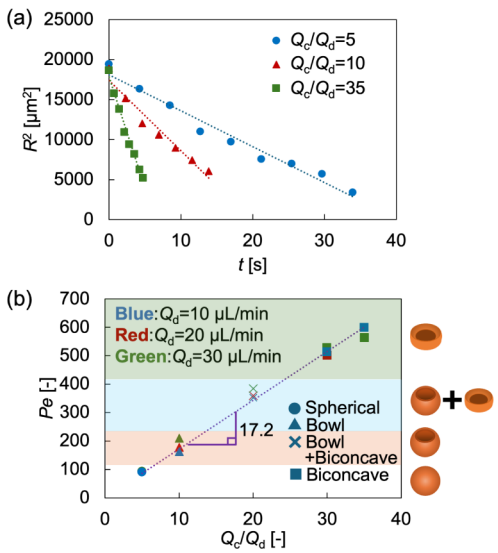

Figure 4. (a) Change in R^2 as a function of time of the droplet prepared with different Q_c/Q_d values: 5 (blue, Q_d = 20 μL/min, Q_c = 100 μL/min), 10 (red, Q_d = 20 μL/min, Q_c = 200 μL/min), and 35 (green, Q_d = 20 μL/min, Q_c = 700 μL/min). The slope of the graph represents droplet shrinkage rate κ. (b) Linear regression between Q_c/Q_d and *Pe*. The symbols of the plots represent the particle shapes: circles denote spherical particles, triangles denote bowl-like particles, crosses denote a mixture of bowl-like and biconcave particles, and squares denote biconcave particles.

rate ratios. *Pe* was calculated using κ according to eq 1; the results are summarized in Table 1. D_p was measured to be 6.16

Table 1. Droplet Shrinkage Rate (κ) and *Pe* at Various Flow Rate Ratios Q_c/Q_d

Flow rate in dispersed phase, Q_d [μL/min]	Flow rate in continuous phase, Q_c [μL/min]	Flow rate ratio, Q_c/Q_d [-]	Droplet shrinkage rate, κ [m^2/s]	Peclet number, *Pe* [-]
20	100	5	4.48×10^{-10}	91.0
	200	10	8.79×10^{-10}	178
	700	35	27.8×10^{-10}	563

$\times 10^{-13}$ m^2/s using the DLS method. *Pe* in the droplet increased with the flow rate ratio because of the increase in κ. At , the droplet interface reduction dominates the diffusion of the polymer, increasing the local polymer concentration near the droplet surface. Consequently, a viscous layer formed near the droplet surface, and the subsequent deformation of the droplet resulted in nonspherical particles. This deformation occurs because solvent diffusion continues even after the viscous layer is formed, causing the volume to decrease. Simultaneously, the surface area of the droplets remains approximately constant owing to vitrification of CA.

We further investigated the relationship among the flow rate ratio, *Pe*, and particle shape by adding the flow rate ratio conditions of 20 and 30. As the flow rate ratio increased, the *Pe* increased linearly, and the particle shape changed from spherical to bowl-like and biconcave. To confirm whether similar results could be obtained with different total flow rates, we investigated the effect of *Pe* on the particle shape by varying the total flow rate while maintaining a constant flow rate ratio. The results of the change in R^2 over time, SEM images of the obtained particles, and *Peunder* all flow rate conditions are summarized in Figure S2 and Table S2. Figure 4b shows that if the flow rate ratio remains constant, the particle shape and *Pe* are almost unaffected by changes in the total flow rate. Mapping the relationship between Q_c/Q_d and particle shape indicated that a viscous layer formed during particle formation at *Pe* greater than 100, resulting in nonspherical particles. It is noted that the threshold *Pe* for particles to become nonspherical from spherical was greater than 1, similar to the findings of Archer et al., where nonspherical shapes were obtained at *Pe* > 26.[40] Then, a linear regression between the flow rate ratio and *Pe* leads to the following correlation equation:

$$Pe = \frac{\kappa}{8D_p} = 17.2\frac{Q_c}{Q_d} \quad (4)$$

eq 4 calculates *Pe* from the initial flow rate ratio, enabling the prediction of whether the resulting particles are spherical or nonspherical, as shown in Figure 4b.

Effect of MA Concentration. To investigate the impact of MA concentration in the continuous phase on the *Pe* and particle shape, MA was added to the continuous phase to achieve MA concentrations in the continuous phase ($c_{MA,\ out}$) of 0, 5, 8, 10, and 25 wt % at Q_c/Q_d = 10 (Q_d = 20 μL/min, Q_c = 200 μL/min). In this case, $c_{MA,\ out}$ of 25 wt % corresponded to the saturation concentration of MA in the continuous phase. Figure 5a shows the time-lapse change of droplets in the microchannel at different $c_{MA,\ out}$, while maintaining a Q_c/Q_d constant at 10. As $c_{MA,\ out}$ increased, the droplets shrank more

https://doi.org/10.1021/acs.langmuir.4c03430
Langmuir 2024, 40, 27314−27322

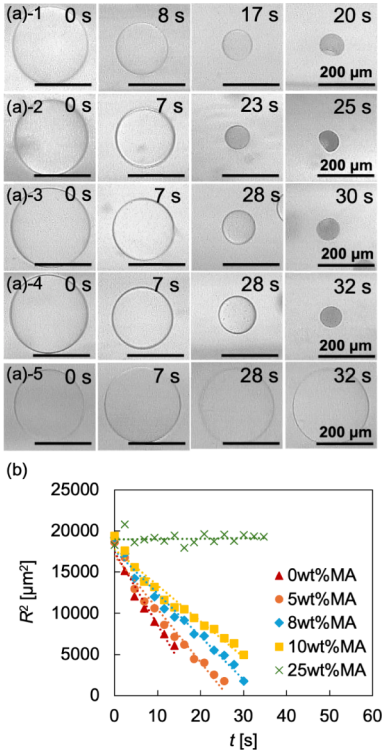

Figure 5. (a) Time-lapse droplet change in a microchannel prepared at different $c_{MA,\ out}$ keeping Q_c/Q_d constant at 10 (Q_d = 20 μL/min, Q_c = 200 μL/min). $c_{MA,\ out}$ values are 0 ((a)-1), 5 ((a)-2), 8 ((a)-3), 10 ((a)-4), and 25 wt % ((a)-5). (b) Change in R^2 as a function of time for the droplet prepared with different $c_{MA,\ out}$. $c_{MA,\ out}$ values are 0 (red), 5 (orange), 8 (bule), 10 (yellow), and 25 wt % (green). The slope of the graph represents droplet shrinkage rate κ.

slowly, and the particle shape changed from nonspherical to spherical. When the MA concentration in the continuous phase was saturated at 25 wt %, the droplets did not shrink and particles were not formed in the microchannel because solvent diffusion did not proceed. The droplet interfacial area (R^2) over time for each MA concentration in the continuous phase (Figure 5b) shows that the slope, which indicates κ, decreases as the MA concentration in the continuous phase increases. The diffusion of MA in the dispersed phase was suppressed according to Fick's law as the concentration gradient of MA between the dispersed and continuous phases decreased, causing the droplets to shrink more slowly. The values of κ and *Pe* at each MA concentration in the continuous phase in Table 2 and the SEM images of the obtained particles in Figure 6 indicated that *Pe* in the droplets decreased as the MA concentration in the continuous phase $c_{MA,\ out}$ increased,

Table 2. Droplet Shrinkage Rate κ and *Pe* at MA Concentration in Continuous Phase, $c_{MA,\ out}$ of 0, 5, 8, 10, and 25 wt %

Flow rate ratio, Q_c/Q_d [-]	MA concentration in continuous phase, $c_{MA,\ out}$ [wt %]	Droplet shrinkage rate, κ [m^2/s]	Peclet number, *Pe* [-]
10	0	8.79×10^{-10}	178
	5	6.45×10^{-10}	131
	8	5.23×10^{-10}	106
	10	4.37×10^{-10}	89.0
	25	-	-

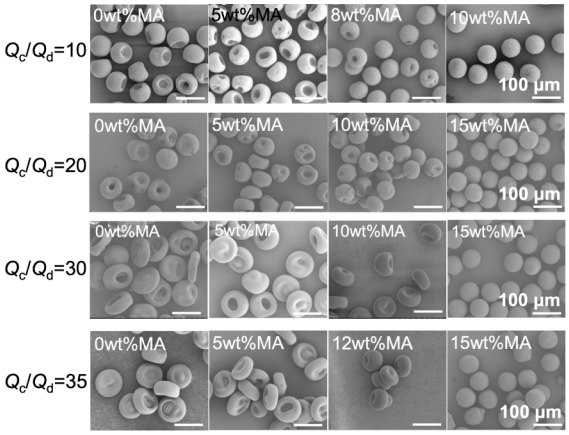

Figure 6. SEM images of CA particles prepared with different Q_c/Q_d and $c_{MA,\ out}$. Q_c/Q_d values are 10, 20, 30, and 35 from the top to bottom. $c_{MA,\ out}$ values are 0, 5, 8, and 10 wt %, 0, 5, 10, and 15 wt %, 0, 5, 10, and 15 wt %, and 0, 5, 10, and 15 wt % when Q_c/Q_d values are 10, 20, 30, and 35, respectively.

resulting in the elimination of polymer concentration gradients during the shrinkage process, and the particle shapes changed from bowl-like to dimpled and then to spherical.

Correlation of *Pe*, Flow Rate Ratio, and MA Concentration. The changes in particle shapes at different $c_{MA,\ out}$ were also investigated at Q_c/Q_d = 20, 30, and 35, as shown in Figure 6. Regardless of the change in the flow rate ratio, the same trend was observed; i.e., the particle shape changed from nonspherical (bowl-like and biconcave) to spherical as $c_{MA,\ out}$ increased. The correlation equation between the flow rate ratio and *Pe* at different MA concentrations in the continuous phase ($c_{MA,\ out}$ = 0, 5, 10, 12, and 15 wt %) is shown in Figure 7a. The plots of the change in R^2 over time, SEM images of the particles and *Pe* prepared with different $c_{MA,\ out}$ (= 0−15 wt %) at various Q_c/Q_d = 5−35 are summarized in Figure S3 and Table S3. We observed that the slopes of these correlation equations decrease as $c_{MA,\ out}$ increases. We examined the relationship between these slopes and the ratio of $c_{MA,\ out}$ to the MA saturation concentration $c^*_{MA,\ out}$, as shown in Figure 7b. Eq 5 indicates that the slopes decrease linearly as the MA concentration increases.

$$\text{slope} = -21.1\frac{c_{MA,out}}{c^*_{MA,out}} + 17.2 \quad (5)$$

The correlation equation between the flow rate ratio, MA concentration in the continuous phase, and *Pe*, as shown in eq 6, was derived by substituting eq 5 into *Pe* = slope × Q_c/Q_d.

$$Pe = -21.1\frac{c_{MA,out}}{c^*_{MA,out}}\frac{Q_c}{Q_d} + 17.2\frac{Q_c}{Q_d} \quad (6)$$

Using this equation, *Pe* in the droplets can be predicted from the initial flow conditions (i.e., the flow rate conditions and continuous phase composition), allowing the prediction of whether the resulting particle shape will be spherical or nonspherical.

Effect of Droplet Position in Microchannels. Figure 8 shows the time-lapse changes in droplets observed from the top and side when bowl-like (Q_c/Q_d = 10, *Pe* = 178) and biconcave particles (Q_c/Q_d = 35, *Pe* = 563) were formed, respectively. From the side view, we found that the droplets

https://doi.org/10.1021/acs.langmuir.4c03430
Langmuir 2024, 40, 27314−27322

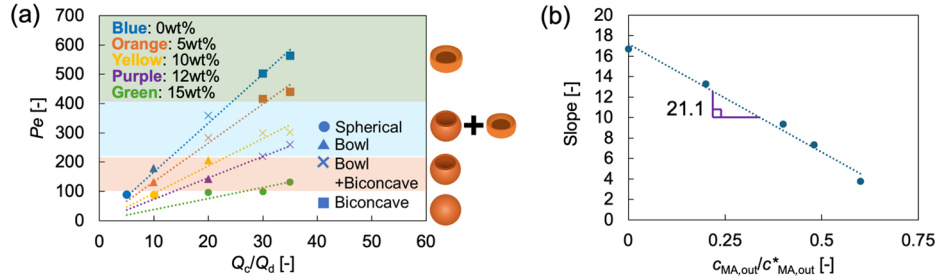

Figure 7. (a) Correlation equation between the flow rate ratio and *Pe* at different MA concentrations in the continuous phase ($c_{MA,\ out}$ = 0−15 wt %). The symbols of the plots represent the particle shapes: circles denote spherical particles, triangles denote bowl-like particles, crosses denote a mixture of bowl-like and biconcave particles, and squares denote biconcave particles. (b) Changes in the slope of the correlation equation between the flow rate ratio and *Pe* as a function of MA concentrations in the continuous phase. $c^*_{MA,\ out}$ represents the MA saturation concentration in the continuous phase.

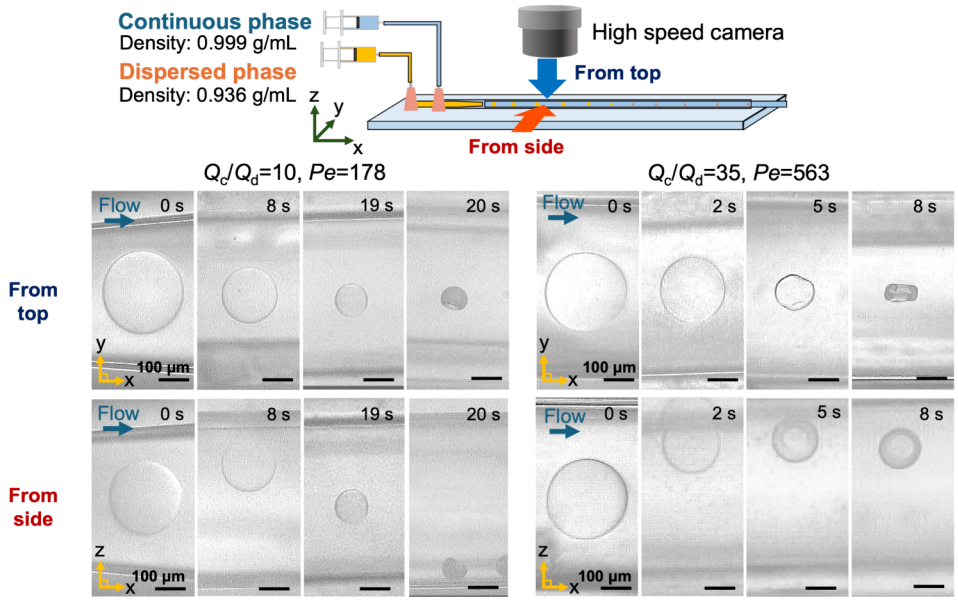

Figure 8. Time-lapse changes of droplets observed from the top and side using a high-speed camera in a microfluidic device. Left: high-speed snapshot at Q_c/Q_d = 10 (*Pe* = 178), and right: high-speed snapshot at Q_c/Q_d = 35 (*Pe* = 563).

rose to the top of the channel shortly after emulsification, driven by the density difference between the dispersed phase (0.936 g/mL) and the continuous phase (0.999 g/mL). As the CA concentration in the droplets increased, owing to MA diffusion, the droplets began to sink and turn cloudy, indicating the formation of a viscous layer. Specifically, at *Pe* = 563, cloudiness became apparent when the droplet remained near the top of the channel. Conversely, at *Pe* = 178, cloudiness was initiated when the droplet reached the center of the channel while sinking from the top. This difference indicated that the position of the droplets within the microchannel affected how the viscous layer was formed. With a high *Pe*, the polymer concentration near the droplet surface increases early during solvent diffusion when the droplet is still large. As the droplet density remained low, a viscous layer formed before the droplet sank. In addition, as the droplet was positioned in the upper part of the microchannel, backward rotation occurred owing to the flow of the continuous phase (Movie S1). This rotation enhanced solvent removal in the rotating direction, forming a viscous layer with a higher polymer concentration. In the direction perpendicular to rotation, a droplet front with a relatively low polymer concentration was formed. This difference in the local polymer concentration in the droplets induced deformation in these two directions, forming biconcave-shaped particles. On the other hand, at low *Pe*, a viscous layer formed when the droplet traveled to the center of the channel during sinking. At this point, there was no influence of rotation owing to the continuous phase flow, resulting in the formation of a viscous layer covering the droplet, and deformation from a random direction led to the formation of bowl-like particles. From these results, we found that the final particle shape was affected by the location of the droplets when the viscous layer was formed.

Relation of *Pe*, Droplet Position, and Particle Shape. Subsequently, we investigated the correlation among *Pe*, droplet location, and particle shape. The location of the droplets during particle formation (z) was defined as the distance from the top of the droplet to the bottom wall of the channel. Figure 9 shows the ratio of the droplet location at the viscous layer formation, z_{layer}/z_{max}, as a function of *Pe*, where z_{layer} is the location of the droplet at the viscous layer formation and z_{max} is the width of the channel. The droplet location during the formation of the viscous layer tended to increase as *Pe* increased, and the particle shape changed from bowl-like to biconcave. The regression line is described in eq 7.

https://doi.org/10.1021/acs.langmuir.4c03430
Langmuir 2024, 40, 27314−27322

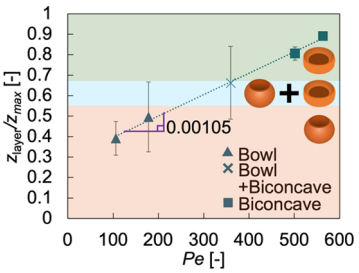

Figure 9. Correlation between *Pe* and droplet location in a microchannel when a viscous layer forms at the droplet surface. z_{layer} and z_{max} represent the location of the droplet within the channel during the formation of the viscous layer and the width of the channel, respectively.

$$z_{layer}/z_{max} = 0.00105Pe + 0.292 \quad (7)$$

Bowl-like particles were obtained when $z_{layer}/z_{max} < 0.55$, a mixture of bowl-like and biconcave particles were obtained when $0.55 < z_{layer}/z_{max} < 0.67$, and biconcave particles were obtained when $z_{layer}/z_{max} > 0.67$. If $Pe > 100$, we can possibly predict whether the shape of the nonspherical particles will be bowl-like or biconcave using eq 7 and the map shown in Figure 9.

Generalizability of This Study. So far, we have examined microparticle preparation under restricted conditions, specifically using a fixed CA concentration, initial droplet diameter, and polymer type. To assess the generalizability of our findings, we investigated the effects of other factors—such as CA concentration in the dispersed phase, initial droplet diameter, and CA molecular weight—on *Pe* and particle shape. First, when varying the CA concentration in the dispersed phase from 0.5 to 3 wt %, we confirmed a decrease in the CA diffusion coefficient due to the increased viscosity of the dispersed phase (Figure S4a). This led to an increase in the *Pe* number within the droplets, with a critical boundary at *Pe* = 100, beyond which the particle shape transitioned from spherical to bowl-shaped or biconcave (Figure S4b). Next, as the initial droplet diameter increased, the shrinkage rate during solvent diffusion also increased (Figure S5a). This resulted in higher *Pe* within the droplets, causing the particle shape to shift from bowl-shaped to biconcave (Figure S5b).

Similarly, changes in the molecular weight of CA in the dispersed phase revealed that higher molecular weights decreased the CA diffusion coefficient due to the slower movement of larger molecules, leading to an increase in *Pe* and a corresponding shape change from bowl-shaped to biconcave (Figure S6). In these cases, a transition from spherical to nonspherical shapes was observed at *Pe* = 100, regardless of the molecular weights of the polymer. Finally, we explored the preparation of particles using polymers other than CA, specifically ethyl cellulose (EC) and poly(D,L-lactide) (PDLLA). Both polymers exhibited nonspherical shapes when *Pe* exceeded 100, similar to CA (Figure S7). However, the resulting particles did not possess the same nonspherical morphology as those formed with CA, suggesting that the final nonspherical shape may be influenced by the mechanical properties and density of the polymer. Additionally, PDLLA, a relatively hydrophilic polymer, produced porous microparticles with an internal structure distinct from that of CA, likely due to water absorption during solvent diffusion. These findings indicate that certain polymers exhibit variations in both the shape and internal structure.

When comparing our results with the previous report,[39] we found that higher water solubility of the solvent is critical for inducing particle deformation, which is in good agreement with the previous research. However, while the molecular weight and concentration of the polymer influenced nonspherical shape formation in the previous report, our findings suggest that particle shape can be better classified based on *Pe* numbers rather than molecular weight or concentration of polymers alone. The technique to selectively produce spherical and nonspherical microparticles by adjusting flow conditions is expected to be crucial for achieving targeted shapes in particle manufacturing processes.

In summary, our results demonstrate that factors such as CA concentration in the dispersed phase, initial droplet diameter, CA molecular weight, and polymer type each affect *Pe* and particle shape. Moreover, even when these parameters were varied, the proposed threshold of *Pe* = 100 generally defined the boundary between spherical and nonspherical shapes. However, since we did not achieve the same nonspherical shapes or internal structures with other polymer systems as we obtained with CA, we conclude that the detailed nonspherical shape transitions (i.e., bowl and biconcave shapes) described by our model may be specific to CA. Further modification of the model will be necessary to broaden its applicability to other polymer systems.

CONCLUSIONS

In this study, we proposed a method for fabricating nonspherical CA microparticles using a microfluidic device and demonstrated the critical role of *Pe* in dictating their morphology. By modulating the flow rate ratios and MA concentration in the continuous phase, we achieved control over the droplet interface dynamics, which, in turn, influenced the *Pe* values significantly. Higher *Pe* values (>100) were associated with the rapid formation of a viscous polymer layer near the droplet interface, leading to the development of nonspherical particles, such as bowl-like and biconcave structures. Our results established two models, i.e., linking the flow rate ratio and MA concentration in the continuous phase with *Pe* and linking *Pe* with the *z*-axis location of droplets at the time of viscous layer formation, enabling the prediction of final particle shapes using *Pe*-structure mapping.

In addition, we explored the effects of other factors, including CA concentration, initial droplet diameter, and CA molecular weight, on *Pe* and particle shape and found that each impacted *Pe* and particle morphology. Across these parameters, *Pe* = 100 emerged as a consistent threshold for the transition from spherical to nonspherical shapes. However, this model appeared partly specific to CA, as other polymers (EC and PDLLA) did not produce the same nonspherical structures, likely due to differences in mechanical properties, hydrophilicity, and density of the polymer.

Overall, these findings underscore the potential of the *Pe* number as a predictive tool for particle shape control in microfluidic systems similar to spray-drying processes, but further modification of the model will be required to broaden its applicability to other polymer systems.

ASSOCIATED CONTENT

Supporting Information

The Supporting Information is available free of charge at https://pubs.acs.org/doi/10.1021/acs.langmuir.4c03430.

https://doi.org/10.1021/acs.langmuir.4c03430
Langmuir 2024, 40, 27314−27322

Photograph of the microfluidic device; junction point of dispersed phase and continuous phase in the microfluidic device; flow rate conditions and collection capillary tip size of a microfluidic device; change in R^2 as a function of time of the droplet prepared with different Q_c/Q_d; SEM images of the particles prepared with different Q_c/Q_d; droplet shrinkage rate κ and Pe when Q_c/Q_d are 5−35; change in R^2 as a function of time of the droplet prepared with different $c_{MA,\ out}$; SEM images of the particles prepared with different $c_{MA,\ out}$; droplet shrinkage rate κ and Pe when $c_{MA,\ out}$ are 0−15 wt %; diffusion coefficients of CA in MA (D_p) at different CA concentrations in the dispersed phase ($c_{CA,in}$); SEM images of CA particles prepared with different $c_{CA,in}$; $c_{CA,in}$ was 0.5 (Pe = 44.6), 1 (Pe = 100), 2 (Pe = 178), and 3 wt % (Pe = 424) from left to right; the junction of the dispersed phase and continuous phases in a microfluidic device at a $c_{CA,in}$ concentration of 3 wt %; change in R^2 as a function of time of the droplet prepared with different initial droplet diameter (D_0); time-lapse droplets change in microchannel SEM images of resultant particles prepared with different D_0; SEM images of resultant particles prepared with different M_w of CA at Q_c/Q_d = 10; SEM images of EC particles prepared with different Pe; SEM images of PDLLA particles prepared with different Pe (PDF)

A video of the droplets in a microfluidic device observed from the side using a high-speed camera when the diffusion time was approximately 5 s at Q_c/Q_d = 35 (MP4)

AUTHOR INFORMATION

Corresponding Authors

Takaichi Watanabe − *Department of Applied Chemistry, Graduate School of Environmental, Life, Natural Science and Technology, Okayama University, Okayama 700-8530, Japan*; orcid.org/0000-0002-5855-2583; Phone: + 81-86-251-8072; Email: wata-t@okayama-u.ac.jp

Tsutomu Ono − *Department of Applied Chemistry, Graduate School of Environmental, Life, Natural Science and Technology, Okayama University, Okayama 700-8530, Japan*; orcid.org/0000-0002-2880-7119; Phone: +81-86-251-8083; Email: tono@okayama-u.ac.jp

Author

Kurumi Mori − *Department of Applied Chemistry, Graduate School of Environmental, Life, Natural Science and Technology, Okayama University, Okayama 700-8530, Japan*

Complete contact information is available at: https://pubs.acs.org/10.1021/acs.langmuir.4c03430

Author Contributions

K.M. and T.W. designed the experiments. K.M. and T.W. performed the experiments and analyzed the data. T.W. and T.O. designed the study. The manuscript was written through contributions of all authors. All authors have given approval to the final version of the manuscript.

Notes

The authors declare no competing financial interest.

ACKNOWLEDGMENTS

This work was financially supported by JSPS KAKENHI (Grant no. JP24K01236 and JP21H01693) and the Young Faculty Promotion Program (2024) of Okayama University.

REFERENCES

(1) Yang, H.; Lu, X.; Xin, Z. One-Step Synthesis of Nonspherical Organosilica Particles with Tunable Morphology. *Langmuir* **2018**, *34* (39), 11723−11728.

(2) Wang, W.; Zhang, M. J.; Xie, R.; Ju, X. J.; Yang, C.; Mou, C. L.; Weitz, D. A.; Chu, L. Y. Hole−Shell Microparticles from Controllably Evolved Double Emulsions. *Angew. Chem., Int. Ed.* **2013**, *52* (31), 8084−8087.

(3) Fei, R.; Wang, H.; Wang, Q.; Qiu, R.; Tang, S.; Wang, R.; He, B.; Gong, Y.; Fan, H. J. In Situ Hard-Template Synthesis of Hollow Bowl-Like Carbon: A Potential Versatile Platform for Sodium and Zinc Ion Capacitors. *Adv. Energy Mater.* **2020**, *10* (47), 2002741.

(4) Jing, J.; Gao, F.; Li, H.; Shi, S.; Huo, H.; Li, C.; An, C. Preparation and characterization of TATB-based energetic composite microspheres by continuous pipe-stream self-assembly technology. *Chem. Eng. J.* **2023**, *471*, 144710.

(5) Wang, D.; Zheng, X.; Chen, X.; Hu, G. Flow-pattern-altered syntheses of core−shell and hole−shell microparticles in an axisymmetric microfluidic device. *Acta Mech. Sin.* **2021**, *37*, 1378−1386.

(6) Ifra; Saha, S. Fabrication of Topologically Anisotropic Microparticles and Their Surface Modification with PH Responsive Polymer Brush. *Mater. Sci. Eng., C* **2019**, *104*, 109894.

(7) Sharma, V.; Szymusiak, M.; Shen, H.; Nitsche, L. C.; Liu, Y. Formation of Polymeric Toroidal-Spiral Particles. *Langmuir* **2012**, *28* (1), 729−735.

(8) Fang, A.; Gaillard, C.; Douliez, J. P. Template-Free Formation of Monodisperse Doughnut-Shaped Silica Microparticles by Droplet-Based Microfluidics. *Chem. Mater.* **2011**, *23* (21), 4660−4662.

(9) Zhang, H.; Tuntanatewin, W.; Ishikura, K.; Sogabe, D.; Sugawara, K.; Tokui, A.; Nakagawa, A.; Okamura, Y. Polymer Discs with High Interfacial Adhesion Fabricated from Hot-Pressing of Microspheres. *ACS Appl. Polym. Mater.* **2020**, *2* (8), 3355−3364.

(10) Zhu, X.; Vo, C.; Taylora, M.; Smith, B. R. Non-spherical micro- and nanoparticles in nanomedicine. *Mater. Horiz.* **2019**, *6*, 1094−1121.

(11) Imagawa, K.; Omura, T.; Ihara, Y.; Kono, K.; Suzuki, T.; Minami, H. Preparation of disk-like cellulose particles. *Cellulose* **2017**, *24*, 3111−3118.

(12) Liu, Y.; Ling, S.; Chen, Z.; Xu, J. Ionic Polymerization-Based Synthesis of Bioinspired Adhesive Hydrogel Microparticles with Tunable Morphologies from Microfluidics. *ACS Appl. Mater. Interfaces* **2024**, *16* (28), 37028−37040.

(13) Matsumiya, K.; Inagaki, N. F.; Ito, T. Fabrication of Drug-Loaded Torus-Shaped Alginate Microparticles and Kinetic Analysis of Their Drug Release. *Langmuir* **2024**, *40* (2), 1247−1256.

(14) Fu, J.; Yang, W.; Hou, L.; Chen, Z.; Qiu, T.; Yang, H.; Li, Y. Enhanced Electromagnetic Microwave Absorption Performance of Lightweight Bowl-like Carbon Nanoparticles. *Ind. Eng. Chem. Res.* **2017**, *56* (40), 11460−11466.

(15) Sun, J.; Cao, C.; Chen, J.; Zhao, W.; Tang, Q.; Jiang, B.; Xu, F.; Zhang, Y.; Ji, Q. Bowl-like Nanoreactors Composed of Packed Gold Nanoparticles Surrounded with Silica Nanosheets for a Photothermally Enhancing Enzymatic Reaction. *ACS Appl. Nano Mater.* **2020**, *3* (11), 11465−11473.

(16) Li, Y.; Cao, S.; Zhang, A.; Zhang, C.; Qu, E.; Zhao, Y.; Chen, A. Carbon and nitrogen co-doped bowl-like Au/TiO2 nanostructures with tunable size for enhanced visible-light-driven photocatalysis. *Appl. Surf. Sci.* **2018**, *445*, 350−358.

(17) Peng, X.; Wu, Z.; Li, Z. A bowl-shaped biosorbent derived from sugarcane bagasse lignin for cadmium ion adsorption. *Cellulose* **2020**, *27*, 8757−8768.

(18) Hu, J.; Wang, X.; Liua, L.; Wu, L. A facile and general fabrication method for organic silica hollow spheres and their excellent adsorption properties for heavy metal ions. *J. Mater. Chem. A* **2014**, *2*, 19771−19777.
(19) Park, J. H.; Han, N.; Song, J. E.; Cho, E. C. A Surfactant-Free and Shape-Controlled Synthesis of Nonspherical Janus Particles with Thermally Tunable Amphiphilicity. *Macromol. Rapid Commun.* **2017**, *38* (3), 1600621.
(20) Kim, D. H.; Woo, H. C.; Kim, M. H. Room-Temperature Synthesis of Hollow Polymer Microparticles with an Open Hole on the Surface and Their Application. *Langmuir* **2019**, *35* (42), 13700−13710.
(21) Vahidkhaha, K.; Bagchi, P. Microparticle shape effects on margination, near-wall dynamics and adhesion in a three-dimensional simulation of red blood cell suspension. *Soft Matter* **2015**, *11*, 2097−2109.
(22) Cooley, M.; Sarode, A.; Hoore, M.; Fedosov, D. A.; Mitragotri, S.; Gupta, A. S. Influence of particle size and shape on their margination and wall-adhesion: Implications in drug delivery vehicle design across nano-to-micro scale. *Nanoscale* **2018**, *10*, 15350−15364.
(23) Sun, X.; Huang, Y.; Chen, M.; Peng, X.; Dou, W. Facile Synthesis of Single-Hole Crosslinked Particles with Embedded Single Bulge by Seeded Emulsion Polymerization. *Macromol. Chem. Phys.* **2018**, *219*, 1800150.
(24) Serra, C. A.; Chang, Z. Microfluidic-Assisted Synthesis of Polymer Particles. *Chem. Eng. Technol.* **2008**, *31*, 1099−1115.
(25) Qiao, S.; Li, S.; Song, Q.; Liu, B. Shape-Tunable Biconcave Disc-Like Polymer Particles by Swelling-Induced Phase Separation of Seeded Particles with Hydrophilic Shells. *Langmuir* **2023**, *39* (3), 1190−1197.
(26) Vehring, R.; Foss, W. R.; Lechuga-Ballesteros, D. Particle formation in spray drying. *J. Aerosol Sci.* **2007**, *38*, 728−746.
(27) Zhou, H.; Pujales-Paradela, R.; Groppe, P.; Wintzheimer, S.; Mandel, K. Tuning the Morphology of Spray-Dried Supraparticles: Effects of Building Block Size and Concentration. *Part. Part. Syst. Charact.* **2022**, *39*, 2200127.
(28) Murakami, H.; Kobayashi, M.; Takeuchi, H.; Kawashima, Y. Preparation of poly(dl-lactide-co-glycolide) nanoparticles by modified spontaneous emulsification solvent diffusion method. *Int. J. Pharm.* **1999**, *187* (2), 143−152.
(29) Imbrogno, A.; Piacentini, E.; Drioli, E.; Giorno, L. Preparation of uniform poly-caprolactone Microparticles by membrane emulsification/solvent diffusion process. *J. Membr. Sci.* **2014**, *467*, 262−268.
(30) Meng, F. T.; Ma, G. H.; Qiu, W.; Su, Z. G. W/O/W double emulsion technique using ethyl acetate as organic solvent: Effects of its diffusion rate on the characteristics of microparticles. *J. Controlled Release* **2003**, *91* (3), 407−416.
(31) Xu, J. H.; Li, S. W.; Tan, J.; Wang, Y. J.; Luo, G. S. Preparation of highly monodisperse droplet in a T-junction microfluidic device. *AichE J.* **2006**, *52*, 3005−3010.
(32) Jeong, W. C.; Lim, J. M.; Choi, J. H.; Kim, J. H.; Lee, Y. J.; Kim, S. H.; Lee, G.; Kim, J. D.; Yi, G. R.; Yang, S. M. Controlled generation of submicron emulsion droplets via highly stable tip-streaming mode in microfluidic devices. *Lab Chip* **2012**, *12*, 1446−1453.
(33) Abate, A. R.; Poitzsch, A.; Hwang, Y.; Lee, J.; Czerwinska, J.; Weitz, D. A. Impact of inlet channel geometry on microfluidic drop formation *Phys. Rev. E* **2009**, *80*, 026310.
(34) Lashkaripou, A.; Rodriguez, C.; Ortiz, L.; Densmore, D. Performance tuning of microfluidic flow-focusing droplet generators. *Lab Chip* **2019**, *19*, 1041−1053.
(35) Watanabe, T.; Ono, T.; Kimura, Y. Continuous fabrication of monodisperse polylactide microspheres by droplet-to-particle technology using microfluidic emulsification and emulsion−solvent diffusion. *Soft Matter* **2011**, *7*, 9894−9897.
(36) Zhang, Y.; Cattrall, R. W.; Kolev, S. D. Fast and Environmentally Friendly Microfluidic Technique for the Fabrication of Polymer Microspheres. *Langmuir* **2017**, *33* (51), 14691−14698.
(37) Sharratt, W. N.; Brooker, A.; Robles, E. S. J.; Cabral, J. T. Microfluidic solvent extraction of poly(vinyl alcohol) droplets: Effect of polymer structure on particle and capsule formation. *Soft Matter* **2018**, *14*, 4453−4463.
(38) Wang, B.; Shum, H. C.; Weitz, D. A. Fabrication of Monodisperse Toroidal Particles by Polymer Solidification in Microfluidics. *ChemPhysChem* **2009**, *10* (4), 641−645.
(39) Ono, T.; Yamada, M.; Suzuki, Y.; Taniguchi, T.; Seki, M. One-step synthesis of spherical/nonspherical polymeric microparticles using non-equilibrium microfluidic droplets. *RSC Adv.* **2014**, *4*, 13557−13564.
(40) Archer, J.; Walker, J. S.; Gregson, F. K. A.; Hardy, D. A.; Reid, J. P. Drying Kinetics and Particle Formation from Dilute Colloidal Suspensions in Aerosol Droplets. *Langmuir* **2020**, *36* (42), 12481−12493.
(41) Jakubczyk, D.; Kolwas, M.; Derkachov, G.; Kolwas, K.; Zientara, M. Evaporation of Micro-Droplets: The Radius-Square-Law Revisited. *Acta Phys. Pol., A* **2012**, *122* (4), 709−716.
(42) Vladisavljević, G. T.; Shahmohamadi, H.; Das, D. B.; Ekanem, E. E.; Tauanov, Z.; Sharma, L. Glass capillary microfluidics for production of monodispersed poly (dl-lactic acid) and polycaprolactone microparticles: Experiments and numerical simulations. *J. Colloid Interface Sci.* **2014**, *418*, 163−170.

https://doi.org/10.1021/acs.langmuir.4c03430
Langmuir 2024, 40, 27314−27322